NEAR EARTH OBJECT IMAGE RESTORATION WITH MULTI-OBJECT ADAPTIVE OPTICS

S. J. Weddell[(1)], **R. M. Clare.**[(1)], **and A. Lambert**[(2)]

[(1)]*Dept. of Electrical & Computer Engineering, University of Canterbury, New Zealand, Email: {steve.weddell, richard.clare}@canterbury.ac.nz*
[(2)]*School of Engineering & Information Technology, UNSW, Canberra, Australia, Email: A-Lambert@adfa.edu.au*

ABSTRACT

This article outlines the design and development of a photometry-based image restoration system of near Earth objects for use with 1 m class optical telescopes. Multi-object adaptive optics is used to reduce the effects of atmospheric distortion for improved image resolution of satellite and large debris objects, without the use of artificial beacons. Using wavefront measurements from several background stars, a machine learning platform can simplify tomographic reconstruction to estimate distortion to improve the resolution of images of near Earth objects over a wide field of view, thus simplifying the need for a complex tracking system and removing reliance on laser guide stars.

Keywords: Space Situational Awareness; Adaptive Optics; Optical Telescopes; Satellite Imaging.

1. INTRODUCTION

The increased participation of orbiting satellites from new space aware countries, such as New Zealand and Australia, have generated significant interest in firstly detecting irregularities of orbiting extended objects, such as low Earth orbit satellites [3] and secondly, in characterising large pieces of space debris using photometric data [15, 26]. The need for enhanced resolution can be achieved using adaptive optics (AO) [12, 38], which can provide real-time compensation of atmospheric turbulence, dramatically improving performance of ground-based telescopes to rival that of space telescopes [33, 9].

Without adaptive optics, the resolution of ground-based telescopes is limited by the severity of turbulence, characterised by Fried's coherence length, r_0 [8]. A diffraction-limited 1 m telescope can theoretically resolve a low Earth orbiting satellite at 500 km down to 0.3 m. However, due to turbulence, where r_0 is typically 5 cm at Mt. John Observatory in New Zealand [20], the same telescope would only be capable of resolving an area over 6m. For a geostationary satellite orbiting at 35,768 km, the diffraction-limited resolution is 22 m, however resolution through a 5 cm coherence cell would be 450 m.

To achieve such improvements, estimating optical aberrations due to atmospheric turbulence is a key requirement. Once acquired, such aberrations can be used to enhance photometric data, in theory, to near diffraction-limited performance. Natural guide stars (NGSs) or laser guide stars (LGSs) can be used as beacons to measure distortion near a target object. Based on a 5% probability of finding a faint ($mv = 12$) or brighter NGS within 145 μrad of a target near the Galactic plane [19], LGSs can be placed near a target, however, technical issues exist, such as the cone effect, where multiple LGSs would need to be positioned to track an exoatmospheric object. Using several background stars as natural beacons, we propose to make use of atmospheric tomography to estimate turbulence anywhere within the metapupil of a telescope over a wide field-of-view. Our group specialises in wide field-of-view imaging and low photon count wavefront sensor designs. Employing this technology, we propose discontinuous tracking of low Earth orbit satellites whilst measuring the distortion function of several NGSs to improve the resolution of photometric data over sequences of an orbiting satellite's trajectory.

Our simulations show that processing independent measurements of turbulence in layers from each NGS is simplified using a trained artificial neural network. A reservoir computer is a recurrent neural network that can be trained with off-axis, anisoplanatic patches [8]. Wide-field wavefront sensors provide NGS phase estimates over a region that may contain a target object. Given *a priori* position and trajectory knowledge of a satellite or a debris field, subsequent tomographic evaluation using reservoir computing and deconvolution can improve resolution. In this paper, we outline a tomographic method to estimate low order aberrations which can be used to restore image and light curve data from extended orbiting objects for detection and classification.

This paper is organised as follows. Firstly, a background on satellite imaging and two approaches, i.e., lucky imaging and adaptive optics for near Earth object and debris detection is presented in the following section. A key requirement for our proposed method is advanced wave-

front sensor technology; this topic is outlined in Section 3 and includes multi-object sensing techniques. In Section 4, a tomographic approach with machine learning is discussed for estimation of the spatially varying point spread function over a wide field-of-view. The application of these approaches to improve image resolution of near Earth objects using multi-object adaptive optics is described in Section 5, and this includes image restoration methodologies on extended objects, such as large satellites and associated components, and space debris objects over 1 m in length. Lastly, this article is concluded in Section 6 and several projects are outlined that comprise future work.
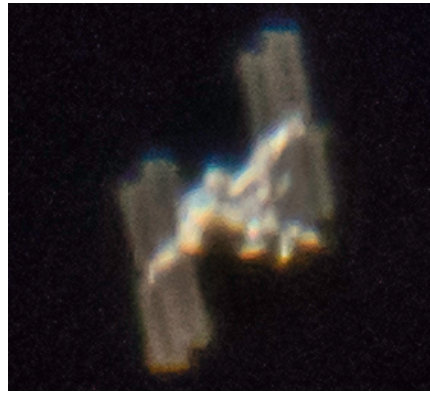

Figure 1. High resolution image of the ISS taken from Mt. John University Observatory by Dr. Ian Griffin.

2. BACKGROUND AND METHODOLOGY

Telescopes can image orbiting or geostationary satellites using reflected sunlight, and this can provide information concerning the general shape of a spacecraft and stability of flight. However, there are two problems using reflected sunlight for high-resolution imaging. Firstly, reflected light is quite different from light generated from a point source, such as a star. Before reaching Earth, the latter wavefront is virtually planar, whereas the former scatters the wavefront, which results in a distorted image. Thus, high resolution images required to show fine, structural details are not possible using just reflected sunlight, due to wavefront phase distortion induced by the Earth's turbulent atmosphere. An artificial LGS [25] can be employed to generate a point source, however several technical challenges exist: (i) LGSs need to be manoeuvred and placed within 15 arcseconds of an approaching satellite [11], (ii) acquisition of low-order aberrations is limited due to the cone effect [36], and (iii) the use of LGSs is restricted in many regions and countries.

Secondly, the number of photons reflected from satellites and space debris is typically very low. For example, since the international space station (ISS) is so large, it can be seen with the unaided eye. However, reflected light from most geostationary satellites, particularly Cubesats, can be several orders of magnitude less than this, and thus, photon levels can be well below the noise floor of most state-of-the-art image detectors. Adaptive optics [38], which can partially correct for the effects of turbulence by compensating the optical path of a telescope in real-time, is an essential requirement. However, AO requires a point source to measure turbulence very near a moving object [3]. Techniques, such as modal tomography [8] can relax the on-axis (close separation) requirement and extend what is known as the isoplanatic patch [32], however NGSs offer a simplified alternative to LGSs, effectively negating the need for their generation, precise placement, and a mechanism to provide manoeuvrability.

2.1. Lucky Imaging

For small aperture telescopes, lucky imaging can be used in order to obtain a highly resolved image, which can show more detail of a satellite. A lucky image is a short-exposure of a point source object through a coherent cell that passes between the object and aperture, and where the RMS wavefront error of 1 rad, over the length of the cell, which is equal to the diameter of the aperture. The coherent length of cells can be characterised for an observation site; the parameter used is Fried's coherence length, r_0 [8]. Variations over time results in performance variation, where individual highly resolved images can be selected for analysis. An example of a highly resolved image of the ISS taken from the University of Canterbury Mt. John Observatory by Griffin is shown in Figure 1. This image was recorded on the 30 th July at 07:35 using the 0.6 M Boller and Chivens telescope at prime focus using a Sony A9 camera with $1/4000$ s exposure and 12800 ISO. The A9 camera was set to "burst" mode, which took 20 frames per second in RAW image format.

From early work by Fried [7], the probability of a lucky frame $p(\text{lucky})$, given a coherent cell size r_0 and aperture of diameter D, can be defined as,

$$p(\text{lucky}) \approx 5.6 \exp[-0.1557(D/r_0)^2]). \qquad (1)$$

A site profile has been performed at Mt. John University Observatory [20], which characterised the turbulence profile by the refractive index structure constant, C_n^2, and determined Fried's parameter to be $r_0 = 5$ cm. Using this parameter, and a telescope aperture of 1 m, the probability of a *lucky* image is, $p(\text{lucky}) \approx 5.02 \times 10^{-27}$. Thus, for this site, the occurrence of a lucky frame would be an extremely rare event. However, with careful selection of highly resolved images, in addition to preprocessing, e.g., the shift and add method, a realisable and significant improvement in image resolution is possible. Hybrid methods, which include a combination of adaptive optics and lucky imaging, have been used for general astronomical imaging. [1].

2.2. Adaptive Optics

Adaptive optics comprises electrical, optical, and mechanical instrumentation and sensor technology, that, when fitted to an optical telescope supported by a computerised control system, can effectively reduce optical aberrations caused by atmospheric turbulence. This is achieved by effectively measuring the distortion using a wavefront sensor, and either changing the optical path in real-time using actuators and flexible mirrors, or estimating the short-exposure point spread function for correction of perturbed images using deconvolution. Given the wealth of literature available in the field of adaptive optics [32, 12, 38] only a brief overview of the main components and our associated contributions will be given here.

A typical AO system can be described using the schematic shown in Figure 2. The wavefront sensor (WFS) provides measurements which are used by the wavefront controller to estimate the instantaneous shape of an incoming wavefront. Based on this estimate of the wavefront, the wavefront controller calculates commands to control the shape of a deformable mirror (DM). A DM is a mirrored surface with an array of actuators attached to the rear of a flexible mirror. The actuators allow the shape of the mirror surface to be changed from planar. If a conjugate of the wavefront shape measured for the ground layer turbulence is output to the DM, the resulting wavefront would emerge as highly corrected; only minor high orders of aberrations would remain, in addition to the upper layer turbulence perturbations, as shown in the lower-middle of the schematic. Lastly, Figure 2 shows two objects; one is a reference star, the other is a science object. Typically, a bright point source reference is used for wavefront measurements when there is insufficient photon flux from a faint science object. However, to ensure the same wavefront is measured for the science object, the angular separation between the reference and object must be within the isoplanatic angle, θ_0 [8]. The next section will discuss our design of a geometric wavefront sensor, which can measure wavefronts from multiple objects, thus extending the isoplanatic angle.

3. MULTI-OBJECT WAVEFRONT SENSORS

A primary motivation for designing a multi-object wavefront sensor is to capture simultaneous samples of atmospheric turbulence over a wide field of view. Using atmospheric tomography [29], the isoplanatic angle referred to in Section 2.2 can be extended. To show how this can be effectively used in the case of a space situational awareness application, the schematic shown in Figure 3 extends the top portion of Figure 2 discussed in Section 2.2.

In order to extend the anisoplanatic angle (the demarcation of the resulting region is known as an isoplanatic *patch*), the multi-object wavefront sensor shown in Figure 4 was developed and tested [42]. The aim of this design is to capture multiple background stars over a
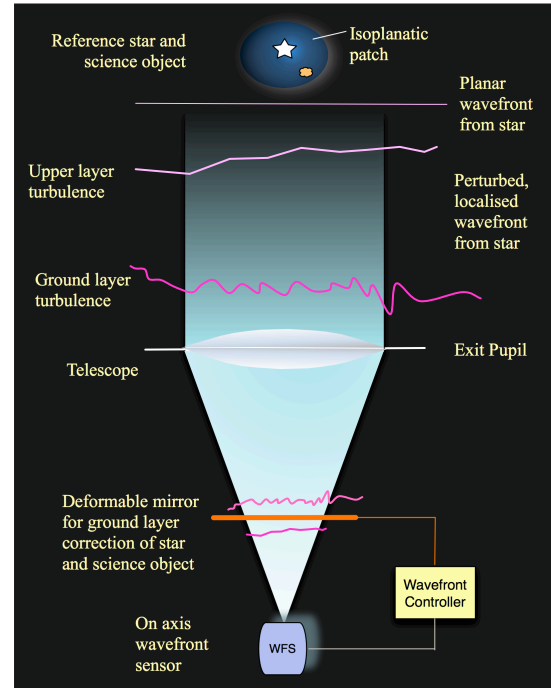

Figure 2. A simplified overview of an adaptive optics system. The wavefront controller reads measurements from the wavefront sensor and computes commands to control a deformable mirror. Control is performed in closed loop to minimise wavefront perturbations.

wide field of view using a simplified method that supports two defocused images, i.e, the intra-focal and extra-focal planes. The general configuration of this wavefront sensor is similar to that of the curvature sensor, which uses the second derivative of intensity measurements to determine wavefront curvature [31, 39, 4]. However, the method used to extract multiple wavefronts is based on slope measurements and is referred to as the *geometric* wavefront sensor [40]. The geometric wavefront sensor has also been called a *two pupil plane position wavefront sensor* or TP3-WFS [6].

Modifications were made to this sensor to simplify both the physical arrangement over the optical path, specifically to accommodate multiple reference objects and target object over a wide field-of-view [42]. However, we have also improved the performance of the original geometric sensor through the use of signal processing methods, such as ridgelets and curvelet transforms [18], to reduce complexity of Radon transformations [28].

An example of multi-object wavefront sensing is shown in Figure 5. Here, intra- and extra-focal pupil plane images of two Jovian moons are shown using two separate cameras, each capturing two reference beacons. Both high-speed cameras were synchronised and frames from both cameras at 60 fps were labeled and streamed to separate computers for batch processing. Methods for extracting optical aberrations from each source depend on the type of wavefront sensor used, and some preprocess-
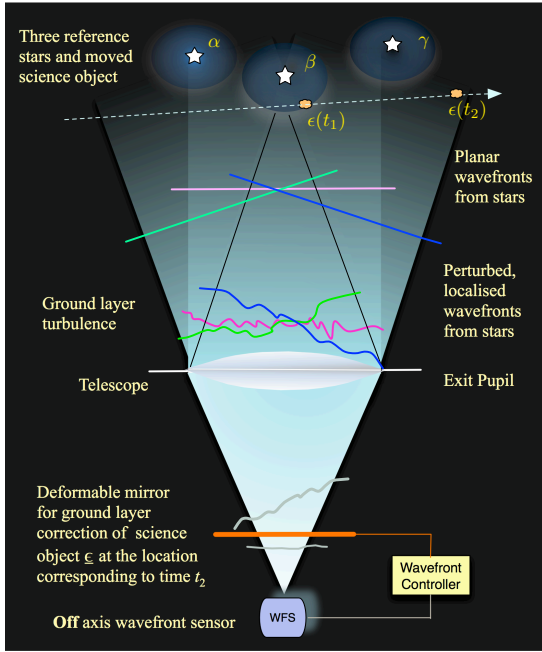
Figure 3. The single source adaptive optics system shown in Figure 2 is extended here to a multi-object adaptive optics system. The zonal regions of several isoplanatic patches are shown and can be captured simultaneously using a wide field of view camera. An example of two temporal instances of a science object, i.e., at time t_1 and t_2, as it moves in to and out of an isoplanatic region, and with respect to three background reference stars, α, β, and γ, is shown. A corrective wavefront to compensate for localised turbulence at the location corresponding to time t_2 of a moving science object, would require a tomographic approach, which would use intra- and extra focal images of all three sources taken simultaneously at time t_2.

ing is required. To obtain phase perturbations, curvature sensors remove scintillation by subtracting the intra-focal from the extra-focal image. Geometric sensors use both images to map the slope of aberrations between pupil plane images and the Radon transform to estimate the displacement [23, 24].

The next section will discuss how a set of aberrations from each reference source, in the form of Zernike polynomials [32], can be combined to achieve high resolution imaging of target objects by reducing the effects of turbulence over anisoplanatic regions.

4. A TOMOGRAPHIC APPROACH WITH MACHINE LEARNING

As discussed in Section 2.2, AO systems can provide image improvement when a science object is within close separation of a bright reference source, such as a natural guide star or a laser beacon. However, such localised estimation of a turbulent region (isoplanatic patch) for image restoration of a science object can be extended by imaging multiple reference sources and by applying tomographic processes. Somewhat ambitiously, multi-object adaptive optics using atmospheric tomography has been proposed for whole sky correction [30].

A brief overview highlighting atmospheric tomography will be covered in this section, and corresponding machine learning methods for simplifying the tomographic matrix will be outlined.

4.1. Atmospheric Tomography

Computerised tomographic imaging [14] is an extensive topic and so only a summary of how modal tomography for AO [29] has been integrated with spatiotemporal modal estimation using known *a posteriori* source aberration data will be covered in this section.

As first proposed by Tallon and Foy [36], the basic idea is to use *a posteriori* estimates of turbulence aberrations from multiple point source objects, such as background guide stars α, β and γ shown in Figure 6, to determine several isoplanatic patches. Based on known turbulence profiles from site testing, the degree of covariance from overlapping patches, in conjunction with the height of the turbulence layer allows one to construct a covariance matrix, known as the tomographic matrix [29]. Such matrices can be solved to estimate turbulent modes in anisoplanatic regions or patches, which provide an estimate of the distortion perturbing the image of a target object, such as ϵ.

Using only one reference, such as guide star γ, target ϵ is limited to isoplanatic angle, $\theta_{\epsilon,\gamma}$. However, by measuring the turbulence over the three isoplanatic patches (shown as circular disks projected as cylinders through turbulent layers, L_1 and L_2) for each guide star, a tomographic matrix can be used to estimate turbulence patches in spatial regions not directly referenced by a guide star.

4.2. Machine Learning for Computational Reduction

Given the large data ensembles generated that require processing, an alternative to tomographic matrix computations was investigated. The structure chosen is a recurrent neural network, referred to in the literature as *reservoir computing* [34]. These stochastic-based networks support a simplified training methodology, where only the reservoir matrix is used in training to provide linear mapping between input and output layers.

A reservoir computer (RC) [16] is currently used to predict a target object wavefront over wide separations. The type of RC used is an echo state network (ESN) [13], which is a form of a recurrent neural network [17]. Typically, ESN structures are configured for prediction, and thus can be extended for training on spatiotemporal data
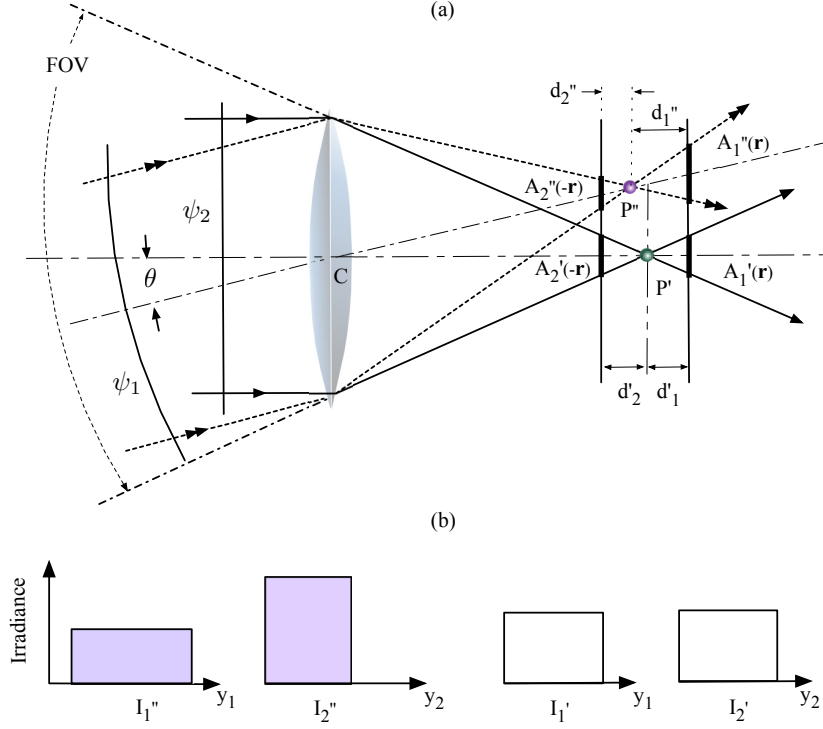
Figure 4. Modified geometric wavefront sensor for multiple object capture: (a) is a geometric projection showing the ray tracing of two wavefronts, each from different objects, where ψ_1 has a defocus aberration and ψ_2 is a planar wavefront; (b) shows the irradiance profiles of the resulting projection on two corresponding pupil planes [42]. The wavefronts are separated by θ μrad.

[41, 42]. A process of mapping isoplanatic regions over a wide spatial region, thus allowing the network to determine the degree of correlation of a set of *4th* order Zernike coefficients in adjacent regions, was devised for training for specific seeing conditions.

An adaptive approach will be required for the network to maintain optimal performance over varying atmospheric conditions [21]. In addition, extended hour angle observations will require additional compensation for higher air mass. Our work considers how this compensation can be achieved, possibility by increasing the number of sources for high air mass observations under GPU acceleration. An ESN was implemented on a GPU for multiple time-step prediction [44].

4.3. Anisoplanatic Imaging Model

In order to reduce computational complexity, an ESN is using to replace the tomographic matrix referred to in Subsection 4.2. In effect, the resulting network shown in Figure 7 is used to learn spatiotemporal mapping and is essentially used to estimate modal perturbations over localised regions. The structure shown was used as a basis for our simulation model and is described in [46]. A summary is given here.

Based on simulations [46] and refined laboratory experi-

ments [45], two short exposure images are captured over a wide field that encompasses three or more source objects, corresponding to NGSs such as α, β, and γ in Figure 3. In the case of three sources, and at time period Δt, a set of noise impaired images comprising regions of interest $\mathbf{I}_{1,2}^1$, $\mathbf{I}_{1,2}^2$, and $\mathbf{I}_{1,2}^3$ are used to estimate a set of N Zernike polynomial coefficients, $\mathbf{Z}_1$, $\mathbf{Z}_2$, and $\mathbf{Z}_3$. Each set, together with separation data ϕ_{Sep} of a target object $\mathbf{Z}_{\text{T}}$, turbulence profile $C_{\mathbf{n}}^2$, and regularisation and other optimising factors are input to an ESN, which has been trained on a similar profile. Spatiotemporal data and parameters are used by the ESN to estimate turbulence aberrations over an anisoplanatic region, A_{T}, but within an isoplanatic region to $\hat{\mathbf{Z}}_{\text{T}}$. Several hundred frames are processed as turbulence is displaced over the aperture forming a time-series for analysis. Lastly, Zernike polynomial coefficient data is taken over the same time-period and are used for comparison, forming a residual phase error.

Unlike the approach taken for atmospheric modal tomography, the ESN method described here does not rely on the construction of a correlation matrix of overlapping pupil data from multiple source objects. The capability to estimate the effects of turbulence, spatiotemporally, and over a wide FOV, is inherently learnt by the ESN through training.

Our method assumes Taylor's frozen flow hypothesis [37], which essentially states that turbulence will effec-
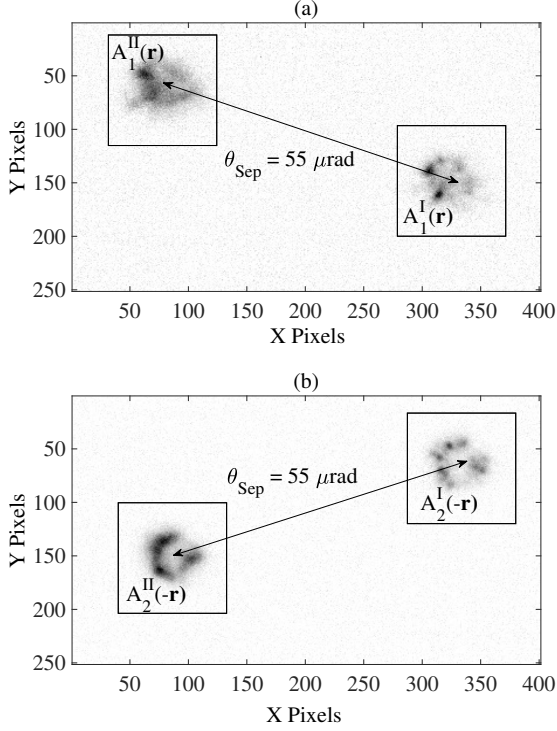
Figure 5. Inverted, defocused images of two Jovian moons Io and Europa, used for wavefront phase experiments: (a) extra-focal image of Io, $A_2''(-\mathbf{r})$ and Europa $A_2'(-\mathbf{r})$; (b): intra-focal image of Io $A_1''(\mathbf{r})$ and Europa $A_1'(\mathbf{r})$.

tively remain "frozen" while passing over the aperture. Short exposure images are acquired to form time-series data; extracted using a multi-object wavefront sensor, each source is separated into Zernike modes. In an experimental study discussed in the next section, we demonstrate how a trained reservoir computer can be used to estimate Zernike modes over intersecting regions within the meta-pupil when a series of similar turbulence conditions are experienced from N natural guide stars.

5. HIGH-RESOLUTION SATELLITE IMAGING

Multiple object AO simulations using astronomical tomography and reservoir computing have been conducted with angular separations, θ_{T}, of $5 < \theta_{\mathrm{T}} < 250\,\mu$rad. An average normalised MSE result for $\theta_{\mathrm{T}} \gg \theta_0$, e.g., $\theta_{\mathrm{T}} = 156\,\mu$rad, using 3 NGSs, 1.3×10^5 photons and 80 db read noise, was reduced to 0.37 of the open-loop error [42]. These simulations currently use batch processing; training data is mostly generated by the simulator but has also been supplemented by both laboratory and field acquisitions. Structures based on a model, which is described in the next subsection, will be formulated to achieve optimal on-sky performance for high-resolution
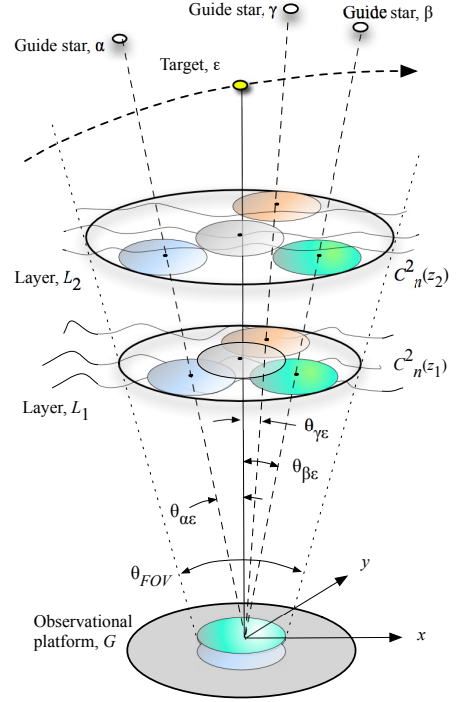

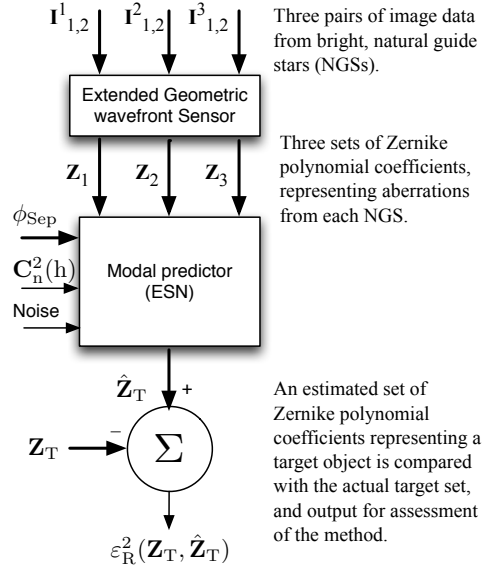*Figure 6. Tomography for multi-object adaptive optics.*

Figure 7. Modal tomographic predictor of Zernike polynomials $\hat{\mathbf{Z}}_T$ employing a trained echo state network [46].

satellite imaging application.

5.1. Tomographic Mapping of Trajectories

A single, annotated, and inverted image frame of the Optus D1 communications satellite, tracked against three
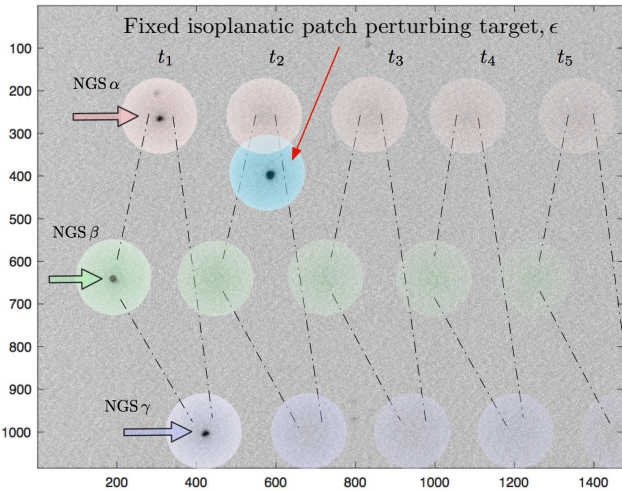
NGSs [27], is shown in Figure 8. This image shows

Figure 8. Annotated satellite image of the Optus D1 satellite with natural stars as background source objects.

the satellite or "target" object as black on a granular light grey background, showing the effect of Gaussian read noise. Three, fainter, natural guide stars are shown, α, β, and γ. The satellite target is being tracked continuously, and remains relatively fixed over several hundred frames. The current frame shows all three background stars and the target object at time t_1. Subsequent frame positions of each star show projected positions of α, β, and γ references, highlighted in pink, green, and purple, respectively, at times t_2, t_3, t_4, and t_5. At each time step a subsequent image captures wavefront perturbations simultaneously from all guide stars and the target object. The isoplanatic circular "patches" of each source object are shown. These regions represent known *a posteriori* perturbations caused by turbulence. Over each updated, wide field-of-view image frame, captured at a frame rate sufficiently high to minimise temporal decorrelation of the changing atmosphere, are used by our multi-object wavefront sensor to determine perturbations from N background stars representing N isoplanatic regions. The resulting data ensembles, used with site profile characteristics [20], effectively map wavefront information using a trained reservoir computer, over the triangular regions shown, i.e., anisoplanatic regions [10], and over each time-step.

Using variants of the K maximum sum, also known as the *bright spot* algorithm [2, 35, 43], the brightest stars within the frame and their positions can be determined. This information allows an n-sided polygon to be constructed, where apexes are formed using n NGSs, and comprises a set of brightest NGSs from each captured frame. Each region can overlap adjacent regions thereby encompassing a region of interest of a target object, or a region where a target is suspected but cannot be detected if below the noise floor due to low photon flux.

Preliminary studies of videos of satellites tracked over a wide field-of-view [27], suggest that between 3 to 10 nat-

ural guide objects of upper limit magnitudes will be available. In terms of percentage of source sky coverage over a reduced field-of-view, estimates based on magnitude, either on- or off-axis from the Galactic centre, appear to correlate with our preliminary estimates [19, 5].

5.2. Restoration Methods on Extended Objects

Distorted images of near Earth Objects taken from ground-based astronomical telescopes resulting from atmospheric turbulence can be partially restored if the aberrations causing the distortion are known. The normalised sum of aberrations forms the point spread function (PSF), which, when deconvolved with a distorted image can partially restore the image. Using perturbed natural, point-source targets, we use atmospheric tomography in an open-loop configuration to estimate the spatially variant point spread function (SVPSF) for image restoration [41]. Thus, deconvolution from wavefront sensing can be applied, where a closed loop, low-order AO corrector can be used to correct PSF tip/tilt displacement in real-time.

Using the SVPSF, we have investigated three widely used image restoration methods: Tikhonov Regularization, Lucy-Richardson and Weiner filtering, and compared these methods [22]. Our analysis, using the full-width at half maximum (FWHM) metric for curvature and geometric wavefront sensors, were assessed from continuous image data in an open-loop configuration. Our results showed that the Lucy-Richardson method had the best performance, in terms of improved FWHM of the restored images for both curvature and geometric wavefront sensors, when compared with the simulated diffraction-limited image. However, the geometric sensor underperformed the curvature sensor over larger propagation distances due to the assumptions of geometric optics breaking down and stronger diffraction effects [4].

6. CONCLUSION AND FUTURE WORK

A simplified method which uses multiple background stars over a wide field-of-view to improve resolution within localised, isoplanatic regions of distorted LEO and GEO images caused by atmospheric turbulence, has been presented. Our proposed method has been simulated and bench-tested in an open-loop configuration as part of a multi-object adaptive optics system. This paper proposes an adaptation of our method to improve the resolution of satellite and space debris images. To achieve this however, the development of new methods for real-time, on sky deployment will be required.

Further testing of our ridgelet-based geometric wavefront sensor (Sect. 3) is required for on sky use. A method is required to maintain relatively consistent irradiance profiles (Sect. 4) from natural point sources, which can vary over several magnitudes, resulting in under and over-exposed geometric slope measurements. We are cur-

rently developing a tip/tilt AO system which will complement our deconvolution from wavefront sensing (Sect. 5) methods, where lucky imaging (Sect. 2.1) may provide further refinement to achieve our ultimate goal of near diffraction-limited resolution performance.

ACKNOWLEDGMENTS

REFERENCES

1. P. L. Aisher, J. Crass, and C. Mackay, "Wavefront phase retrieval with non-linear curvature sensors," *Monthly Notices of the Royal Astronomical Society*, vol. 429, no. 3, pp. 2019–2031, 2013.

2. S. E. Bae and T. Takaoka, "Algorithms for the problem of K maximum sums and a VLSI algorithm for the K maximum subarrays problem," *Parallel Architectures, Algorithms, and Networks, International Symposium on*, p. 247-253, 2004.

3. F. Bennet, C. D'Orgeville, I. Price, F. Rigaut, I. Ritchie, and C. Smith, "Adaptive optics for satellite imaging and space debris ranging," in *Proceedings of the Advanced Maui Optical and Space Surveillance Technologies Conference, Maui, Hawaii, September 15-18, 2014*, vol. 1, p. 2, 2015.

4. T. Y. Chew, *Wavefront sensors in Adaptive Optics*. PhD thesis, Dept. of Electrical & Computer Engineering, University of Canterbury, 2008.

5. R. M. Clare and B. L. Ellerbroek, "Sky coverage estimates for adaptive optics systems from computations in Zernike space," *J. Opt. Soc. Am. A*, vol. 23, pp. 418–426, Feb 2006.

6. C. Colodro-Conde, S. Velasco, R. Lpez, A. Oscoz, Y. Martn-Hernando, R. Rebolo, A. Prez-Garrido, J. Jos Ferrndez-Valdivia, L. Labadie, C. Mackay, M. Puga, G. Rodrguez-Coira, L. Fernando Rodrguez-Ramos, and J. Manuel Rodrguez-Ramos, "The tp3-wfs: a new guy in town," 01 2017.

7. D. L. Fried, "Probability of getting a lucky short-exposure image through turbulence∗," *J. Opt. Soc. Am.*, vol. 68, pp. 1651–1658, Dec 1978.

8. D. L. Fried., "Anisoplanatism in adaptive optics," *J. Opt. Soc. Am.*, vol. 72, pp. 52 – 61, 1982.

9. H. Ferguson, "Space-based vs. ground-based telescopes with adaptive optics (AO)," 2002. Space Telescope Science Institute, Association of Universities for Research in Astronomy (AURA).

10. T. Fusco, J.-M. Conan, L. M. Mugnier, V. Michau, and G. Rousset, "Characterization of adaptive optics point spread function for anisoplanatic imaging. Application to stellar field deconvolution," *Astronomy and Astrophysics*, vol. 142, pp. 149–156, Feb. 2000.

11. D. Grosse, F. Bennet, M. Copeland, C. D'Orgeville, F. Rigaut, and I. Price, "Adaptive optics for satellite imaging and earth based space debris," in *Proceedings of the 7th European Conference on Space Debris, held in Darmstadt, Germany, April 18-21, 2017, Ed.: T. Flohrer and F. Schmitz*, ESA Space Debris Office, 2017.

12. J. W. Hardy, *Adaptive optics for astronomical telescopes*. New York, NY, USA: Oxford University Press., 1998.

13. H. Jaeger, "The echo state approach to analysing and training recurrent neural networks," Tech. Rep. GMD Report 148, German National Research Center for Information Technology, 2001.

14. A. Kak and M. Slaney, "Principles of computerized tomographic imaging," 1988.

15. R. Linares, F. Leve, M. Jah, and J. Crassidis, "Space object mass-specific inertia matrix estimation from photometric data," in *Guidance and Control 2012 - Advances in the Astronautical Sciences*, vol. 144, pp. 41–54, 12 2012.

16. M. Lukoševičius and H. Jaeger, "Overview of reservoir recipes," Technical Report 11, School of Engineering and Science, Jacobs University Bremen, 2007.

17. M. Lukoševičius and H. Jaeger, "Reservoir computing approaches to recurrent neural network training," *Computer Science Review*, vol. 3, pp. 127–149, August 2009.

18. J. Ma and G. Plonka, "The curvelet transform," *IEEE Signal Processing Magazine*, vol. 27, pp. 118–133, March 2010.

19. P. C. McGuire, D. G. Sandler, M. Lloyd-Hart, and T. A. Rhoadarmer, "Adaptive optics: Neural network wavefront sensing, reconstruction, and prediction," *Scientific Applications of Neural Nets, Proceedings of the 194th W. E. Heracus Seminar, 1998*, p. 97, 1999.

20. J. L. Mohr, R. A. Johnston, and P. L. Cottrell, "Optical turbulence measurements and models for Mount John University Observatory," *Publications of the Astronomical Society of Australia*, vol. 27, no. 3, pp. 347–359, 2010.

21. J. Osborn, F. J. D. C. Juez, D. Guzman, T. Butterley, R. Myers, A. Guesalaga, and J. Laine, "Using artificial neural networks for open-loop tomography," *Opt. Express*, vol. 20, pp. 2420–2434, Jan 2012.

22. S. Pal, A. Lambert, and S. Weddell, "Comparison of restoration methods for deconvolution from wavefront sensing (dwfs)," in *Imaging and Applied Optics 2016*, p. AOT2C.3, Optical Society of America, 2016.

23. S. Pal, A. Lambert, R. Clare and S. J. Weddell, "Wavefront sensor optimisation with ridgelets for astronomical image restoration," in *in proceedings of Image & Vision Computing NZ 2017 (IVCNZ'17)*, Christchurch, *in press*, Dec 2017.

24. S. Pal, A. Lambert, R. Clare, and S. J. Weddell, "Wavefront sensor optimisation with ridgelets for astronomical image restoration," vol. *in press*, Proceedings of SPIE, Adaptive Optics Systems VI, 2018.

25. R. R. Parenti and R. J. Sasiela, "Laser-guide-star systems for astronomical applications," *J. Opt. Soc. Am. A*, vol. 11, no. 1, pp. 288–309, 1994.

26. M. Cegarra Polo, I. Vaughn, A. Alenin, and A. Lambert, "On-sky evaluation of passive polarimetry as a technique to characterise space debris," in *Proceedings of the 7th European Conference on Space Debris, Darmstadt, Germany, April 18-21, 2017*, ESA Space Debris Office, 2017.

27. M. C. Polo and A. Lambert, "Optus D1 satellite video, UNSW in Canberra."

28. J. Radon, "On the determination of functions from their integral values along certain manifolds," *IEEE Transactions on Medical Imaging*, vol. 5, pp. 170–176, Dec 1986.

29. R. Ragazzoni, E. Marchetti, and F. Rigaut, "Modal tomography for adaptive optics," *Astron. Astrophys.*, vol. 342, pp. L53–L56, 1999.

30. R. Ragazzoni, E. Marchetti, and G. Valento, "Adaptive-optics corrections available for the whole sky," *Nature (UK)*, vol. 403, no. 6765, pp. 54 – 6, 2000/01/06.

31. F. Roddier. Curvature sensing and compensation: a new concept in adaptive optics. *Applied Optics*, 27(7):1223–1225, 1988.

32. M. C. Roggemann and B. Welsh, *Imaging Through Turbulence*. CRC Press, 1996.

33. G. Schneider, "Domains of observability in the near-infrared with HST/NICMOS and adaptive optics augmented large ground-based telescopes," 2002. A summary study solicited by STScI in preparation for HST Cycle 12, University of Arizona.

34. B. Schrauwen, D. Verstraeten, and J. V. Campenhout, "An overview of reservoir computing: theory, applications and implementations," in *Proceedings of the 15th European Symposium on Artificial Neural Networks*, pp. 471–482, 2007.

35. M. Thaher and T. Takaoka, "Efficient algorithm for the K-maximum convex sum problem," in *Proceedings of ICCS 2010, Procedia CS 1(1)*, pp. 1475–1483, 2010.

36. M. Tallon and R. Foy, "Adaptive telescope with laser probe - Isoplanatism and cone effect," *Astronomy and Astrophysics*, vol. 235, pp. 549–557, Aug 1990.

37. G. I. Taylor. Statistical Theory of Turbulence. *Royal Society of London Proceedings Series A*, 151:421–444, September 1935.

38. R. K. Tyson, *Introduction to Adaptive Optics*. Optical Engineering, IEEE Press, 2000.

39. M. A. van Dam and R. G. Lane, "Extended analysis of curvature sensing," *J. Opt. Soc. Am.*, vol. 19, no. 7, pp. 1390–1397, 2002.

40. M. A. van Dam and R. G. Lane, "Direct wavefront sensing using geometric optics," vol. 4825, Proceedings of SPIE, High Resolution Wavefront Control: Methods, Devices and Applications IV, 2002.

41. S. J. Weddell and R. Y. Webb, "Reservoir computing for prediction of the spatially-variant point spread function," *Selected Topics in Signal Processing, IEEE Journal of*, vol. 2, pp. 624–634, Oct. 2008.

42. S. J. Weddell, *Optical Wavefront Prediction with Reservoir Computing*. PhD thesis, Dept. of Electrical & Computer Engineering, University of Canterbury, 2010.

43. S. J. Weddell, T. Takaoka, T. Read, and R. Candy, "Maximum subarray algorithms for use in optical and radio astronomy," *Journal of Electronic Imaging*, vol. 8500, 10 2012.

44. T. Keith and S. J. Weddell, "The echo state network on the graphics processing unit," in *Proceedings of Artificial Intelligence and Soft Computing. ICAISC 2013. Lecture Notes in Computer Science*, vol. 7894, Springer, Berlin, Heidelberg, 2013.

45. S. J Weddell and A. Lambert, "Optical test-benches for multiple source wavefront propagation and spatiotemporal point-spread function emulation," Applied Optics, vol. 53, 2014.

46. S. J. Weddell and P. J. Bones, "Wavefront prediction with reservoir computing for minimizing the effects of angular anisoplanatism," *Appl. Opt.*, vol. 57, pp. 7140–7151, Sep 2018.